Check for updates

Xuan Zhang
INM—Leibniz Institute for New Materials,
Campus D2 2,
66123 Saarbrücken, Germany
e-mail: xuan.zhang@leibniz-inm.de

Yue Wang
INM—Leibniz Institute for New Materials,
Campus D2 2,
66123 Saarbrücken, Germany
e-mail: yue.wang@leibniz-inm.de

René Hensel
INM—Leibniz Institute for New Materials,
Campus D2 2,
66123 Saarbrücken, Germany
e-mail: rene.hensel@leibniz-inm.de

Eduard Arzt[1]
INM—Leibniz Institute for New Materials,
Campus D2 2,
66123 Saarbrücken, Germany;
Department of Materials Science and Engineering,
Saarland University,
Campus D2 2,
66123 Saarbrücken, Germany
e-mail: eduard.arzt@leibniz-inm.de

A Design Strategy for Mushroom-Shaped Microfibrils With Optimized Dry Adhesion: Experiments and Finite Element Analyses

Enhanced dry adhesion of micropatterned polymeric surfaces has been frequently demonstrated. Among the design parameters, the cap geometry plays an important role to improve their performance. In this study, we combined experiments on single polyurethane mushroom-shaped fibrils (with a stalk diameter of 80 μm and height of 125 μm) against flat glass, with numerical simulations implementing a cohesive zone. We found that the geometry of the mushroom cap strongly affects the interfacial crack behavior and the pull-off stress. The experimental and numerical results suggest that optimal adhesion was accompanied by the appearance of both edge and interior interfacial cracks during separation. Finite elemental analyses revealed the evolution of the interfacial stress distributions as a function of the cap thickness and confirmed the distinct detachment mechanisms. Furthermore, the effect of the stalk diameter and the Young's modulus on the adhesive force was established, resulting in an optimal design for mushroom-shaped fibrils.
[DOI: 10.1115/1.4049183]

Keywords: bio-inspired adhesion, mushroom-shaped fibril, cohesive zone model

Downloaded from http://asmedigitalcollection.asme.org/appliedmechanics/article-pdf/88/3/031015/6624836/jam_88_3_031015.pdf by guest on 20 August 2022

1 Introduction

The development of new automated production lines and the realization of crawling and climbing robots continue to emerge rapidly. Equipped with micropatterned adhesives, functionalities can be further extended to afford the next generation of automated pick-and-place handling [1] or will allow climbing robots more flexibility to locomote, as shown by the Menrva lab at Simon Fraser University [2] or the Cutkosky lab at Stanford University [3]. Micropatterned adhesives typically outperform nonpatterned flat adhesives made from the same material due to several advantages subsumed under "contact splitting effects" [1].

Among the design parameters, the geometry of the cap is most important as it controls the adhesive contact and transmits the stresses to the substrate when the adhesive is loaded. Inspired from nature, several cap designs such as spatula, mushroom-shaped, or even cupped microstructures were discussed over the past years [4–8], which initiated experiments on varying cap geometries of synthetic micropatterned adhesives. These experiments have confirmed that the cap design has a significant role in controlling and enhancing the performance of such adhesives [9–16]. In particular, mushroom-shaped caps clearly outperformed cylindrical microstructures without a specific cap design (i.e., a flat punch design) [9,10]. A mushroom-shaped cap typically consists of a cap that extends the punch diameter laterally at the end of a cylindrical punch (Fig. 1(*a*)). Experimentally, this can be realized by micromachining a mold for a subsequent replication into the desired elastomer, e.g., Ref. [15], or by a dipping method, e.g., Ref. [17]. From previous experiments, it is empirically known that the detachment can vary, as a function of the size of the mushroom, between interfacial cracks that propagate from the edge or the interior of the contact; however, a systematic variation and optimization based on a more quantitative understanding is still missing [15,18,19].

From the contact theory, one can start from a flat punch without a mushroom cap adhering to a rigid half-space. Following previous approaches based on interfacial fracture mechanics [20], it is well known that the failure of the adhesive contact is dominated by the stress singularity at the circumferential edge of the punch. The singular tensile stress σ_{yy} along the interface between the punch (made from an incompressible, elastic material) and the rigid substrate is quantified as follows [20]:

$$\sigma_{yy} = H_1 r^{-0.406} \tag{1}$$

where H_1 is the singularity amplitude and r is the distance from the edge of the punch. Due to the presence of the singularity, the crack and therefore detachment start always from the circumferential edge of the punch. This behavior is expected to break down for very small punch diameters at which detachment becomes insensitive to defects. For such small contacts, detachment should occur simultaneously across the entire interface upon exceeding the cohesive adhesion strength [21,22]. In realistic pillar structures, the edge will have a finite radius of curvature; this will remove the initial singularity but add a small starter crack that then propagates in a singular field [20].

This theory was extended to mushroom-shaped fibrils, where a cap with constant thickness is added to the end of the punch. Spuskanyuk et al. [23] first discussed how the mushroom cap affected the stress singularity under frictionless, sticking, and no-slip boundary conditions. Carbone et al. [24] used the finite element analysis (FEA) to obtain the interfacial stress distribution of the adhesive contact and calculate the pull-off stress by implementing the generalized Griffith condition, where the adhesive stress scales with the crack length $a^{-0.5}$. Balijepalli et al. [25] focused on the edge stress singularity under no-slip condition and found that the singularity was alleviated due to the presence of the mushroom cap; the effect increased for thinner mushroom caps and resulted in higher predicted adhesion stresses. For a

[1]Corresponding author.

Contributed by the Applied Mechanics Division of ASME for publication in the Journal of Applied Mechanics. Manuscript received October 1, 2020; final manuscript received November 13, 2020; published online December 17, 2020. Assoc. Editor: Noy Cohen.

Copyright © 2020 by ASME; reuse license CC-BY 4.0

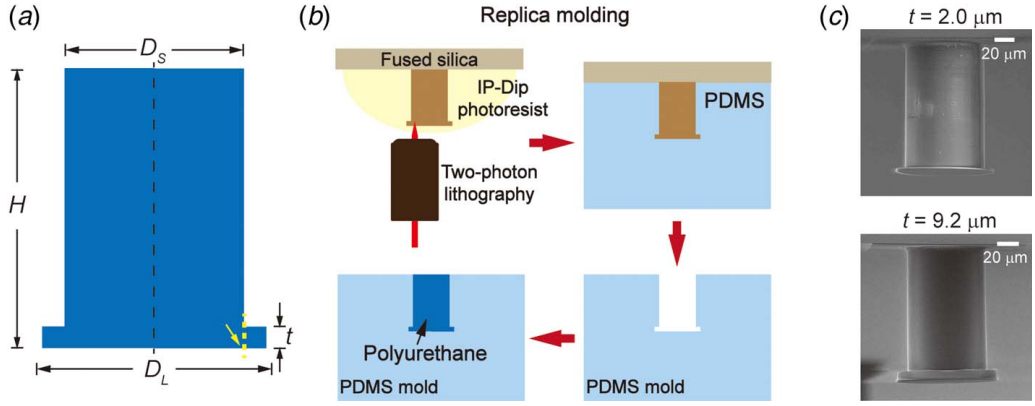

Fig. 1 Fabrication of mushroom-shaped fibrils: (*a*) illustration of the mushroom-shaped fibril model with the fibril height *H*, the stalk diameter D_S, the cap diameter D_L, and the mushroom cap thickness *t*; (*b*) schematic of the microfabrication process that comprises two-photon lithography and replica molding using a silicone (PDMS) mold to obtain mushroom-shaped fibrils made from polyurethane; and (*c*) scanning electron micrographs of individual fibrils with the actual cap thicknesses of $t = 2.0$ μm and $t = 9.2$ μm

conically shaped mushroom cap, Aksak et al. [26] introduced a cohesive zone model into the numerical simulations to optimize the conical cap shape for normal adhesion and found that both the edge angle and the ratio of punch diameter to the cap diameter affected the adhesive force. The implementation of the cohesive zone model allowed them to obtain numerically pull-off forces directly from the simulation results.

In this study, we consider the case of a compliant mushroom-shaped fibril adhering to a stiff flat substrate in both experiments and the FEA by implementing a cohesive zone model to simulate adhesion. This study focuses on the thickness of the mushroom cap and the ratio of the stalk diameter to the mushroom cap diameter. Furthermore, the location of the initial crack and its propagation and the evolution of the interfacial stress distribution provides further insight into the characteristics of different cap design. Finally, we propose a simulation-based guideline for the optimal design of mushroom-shaped adhesives.

2 Experimental Methods

2.1 Fabrication and Characterization. We fabricated single fibrils with mushroom caps using a replica molding process [14], as illustrated in Fig. 1. Master templates with different fibril designs were created using Inventor (Autodesk, San Rafael, CA) and printed by using the two-photon direct laser lithography system Photonic Professional GT (Nanoscribe, Karlsruhe, Germany). The single fibrils had a stalk diameter, $D_S = 80$ μm; a fibril height, $H = 125$ μm; a cap diameter, $D_L = 100$ μm; and cap thicknesses *t* ranging from 2 to 10 μm. For printing, the commercial photoresist IP-Dip (Nanoscribe, Karlsruhe, Germany) in dip-in mode, a writing speed of 10 mm/s, a laser power of 27 mW, and 63 × objective were used. After development and post-curing [27], the fibril designs were transferred into elastomeric polyurethane (PU) by replica molding: First, the master templates were coated with (1H,1H,2H,2H-perfluorooctyl)-trichlorosilane (AB111444, ABCR, Karlsruhe, Germany) by a vapor deposition method for 30 min. Then, the two-part polydimethylsiloxane (PDMS; Sylgard 184, Dow Corning, Midland, MI) was mixed homogeneously in 10:1 mass ratio of base and curing agent. The mixture was poured onto the master templates and cured in an oven at 95 °C for 1 h. After demolding, the PDMS molds were used to replicate the fibrils into PU. The two-part PU (PMC®-770, KauPo Plankenhorn eK, Spaichingen, Germany) was mixed in 2:1 mass ratio of component A to B and, subsequently, poured onto the PDMS molds. To ensure complete filling of the molds, they were degassed at about 1 mbar for 1 h before curing in an oven at 65 °C for 12 h. Upon demolding, the PU microstructures were used for adhesion tests without further treatments. Microstructures were characterized using the scanning electron microscope Quanta 400 (FEI, Hillsboro, OR) to analyze the actual sizes of D_S, D_L, *t*, and *H*, which slightly deviated from the original design due to polymer shrinkage in the fabrication process.

2.2 Adhesion Tests. The adhesion of at least two microfibrils for each cap thickness was tested using a custom-made setup [14]. The setup was composed of a 6 nm step motor Q-545.240 (PI, Karlsruhe, Germany) for vertical displacement and two goniometers, which allowed alignment corrections. The flat glass probe was connected to a bending beam force sensor KD45-2 N (ME-Meßsysteme GmbH, Henningsdorf, Germany). For in situ observations of the contact area and the detachment process, a camera DMK 33UX252 (ImagingSource, Bremen, Germany) with the 12x UltraZoom (Navitar Inc., New York, NY) was used. For illumination, a monochromatic light source with a wavelength of 623 nm was used. Each adhesion test included the approach, hold at compressive preload and retraction until detachment. The approaching rate for all samples was 5 μm/s. The contact was held for 10 s at the preload before retraction at a rate of 0.625 μm/s, which is equal to a strain rate of 5×10^{-3} /s (dividing the actual fibril length by the fibril height). The maximum tensile force was defined as the pull-off force. Each microfibril was tested four times with compressive preloads of 1, 2, 3, and 4 mN.

3 Finite Element Analysis and Cohesive Zone Models

FEAs using ABAQUS [28] were carried out to identify potential mechanisms leading to the detachment of mushroom fibrils with different cap sizes. The axisymmetric model of the mushroom fibril is illustrated in Fig. 2(*a*). The cap diameter was fixed to 10 mm to ensure flaw-sensitive conditions (more details in Discussion section). The ratio of the stalk to cap diameter D_S/D_L was chosen as 0.6, 0.7, 0.8 (as in the experiments), and 0.9. The ratio of the cap thickness to the cap diameter t/D_L ranged from 0.008 to 0.13 (compared to 0.02–0.1 in the experiments). Due to high stress gradients, both the cap close to the interface at the edge and below the transition from the stalk to the cap were meshed using finer seeds. A layer of cohesive elements was inserted at the interface to simulate adhesion and the detachment at critical loading. To mimic attachment of the fully adhered fibril, a no-slip boundary condition was chosen as in the earlier studies [23,25]. The fibril was modeled as an incompressible neo-Hookean elastic

Downloaded from http://asmedigitalcollection.asme.org/appliedmechanics/article-pdf/88/3/031015/6624836/jam_88_3_031015.pdf by guest on 20 August 2022

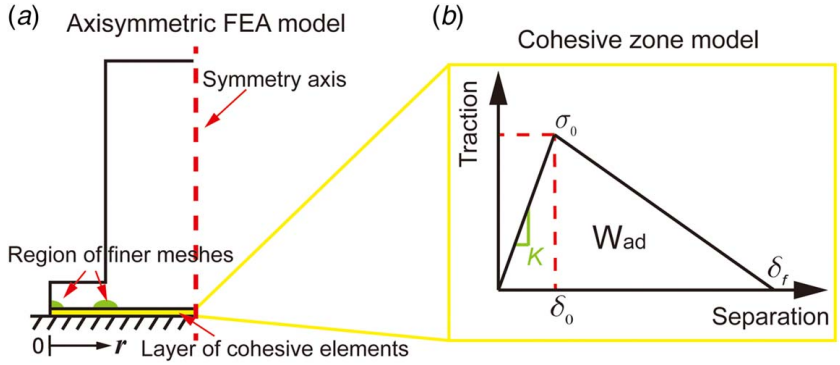

Fig. 2 The finite element model: (*a*) illustration of the axisymmetric model of the mushroom cap fibril contacting with a layer of cohesive elements (the thin layer at the bottom marked by the arrow) to mimic the detachment from a rigid substrate and (*b*) traction-separation law for the cohesive zone model used in the FEA model, where K is the contact stiffness, σ_0 is the maximum traction, δ_0 is the separation when σ_0 reached, δ_f is the maximum separation, and W_{ad} is the delamination energy per unit area

solid with a Young's modulus of 2.52 MPa in accordance to the experiments; there, the Young's modulus of the PU was determined by fitting the linear slope to the force–displacement curve during retraction. The fibril was loaded by applying a uniformly distributed displacement normal to the top surface of the stalk. The reaction force was tracked until it dropped to zero, implying the separation of the fibril from the substrate. The highest reaction force was defined as the pull-off force.

The cohesive zone model was defined as a relative traction-separation response. In ABAQUS, the traction-separation model assumes a linear elastic behavior at the beginning followed by the nucleation and evolution of damage. In this study, a bilinear cohesive zone model was imposed onto the cohesive elements, as shown in Fig. 2(*b*). The adhesion energy per unit area, W_{ad}, is defined as the area integral of the traction-separation curve. In the bilinear model, the interface starts to fail when the separation δ_0 is reached and the maximum traction σ_0 occurs. Full detachment is achieved when the maximum separation δ_f is reached. Separation of the adhesive contact is characterized by a damage parameter D, ranging from 0 to 1. The value is calculated for each cohesive zone element during the simulation as follows:

$$D = \begin{cases} 0, & \delta < \delta_0 \\ \dfrac{\delta_f(\delta - \delta_0)}{\delta(\delta_f - \delta_0)}, & \delta \geq \delta_0 \end{cases} \tag{2}$$

where D is equal to 1 for $\delta = \delta_f$. At this moment, the corresponding cohesive element is deleted. Complete detachment refers to the condition that all the cohesive elements are deleted. In this study, the following parameters were set in the simulations: $W_{ad} = 50$ mJ/m^2, $\sigma_0 = 0.04$ MPa, and the contact stiffness, $K = 400{,}000$ N/mm. The selection of σ_0 and K on the pull-off force is discussed in Appendix A.

4 Experimental Results

Figure 3(*a*) summarizes typical force–displacement curves of microfibrils with various cap thicknesses. During compression (negative forces), approach, and retraction, the curves overlapped, demonstrating low viscoelasticity of the polyurethane with a typical viscoelastic loss factor of $\tan\delta = 0.05$. Pull-off forces varied as a function of the mushroom cap thickness t, with a maximum of 3.14 mN for $t = 5.5$ μm, as displayed in Fig. 3(*b*). It should be noted that the pull-off stress, σ_{Pull}, was calculated from the pull-off force by dividing the actual contact area using the actual $D_L = 97.5 \pm 1.4$ μm measured from scanning electron microscopic images. Thus, the maximum corresponds to a maximum pull-off stress of 0.40 ± 0.07 MPa. The x- and y-axis error bars represent the standard deviations of t and σ_{Pull}, respectively. It is seen that the increase that can be realized is roughly by a factor of 2, while the loss of adhesion for thinner caps is less pronounced. Considering that the cap thickness was changed as the only variable

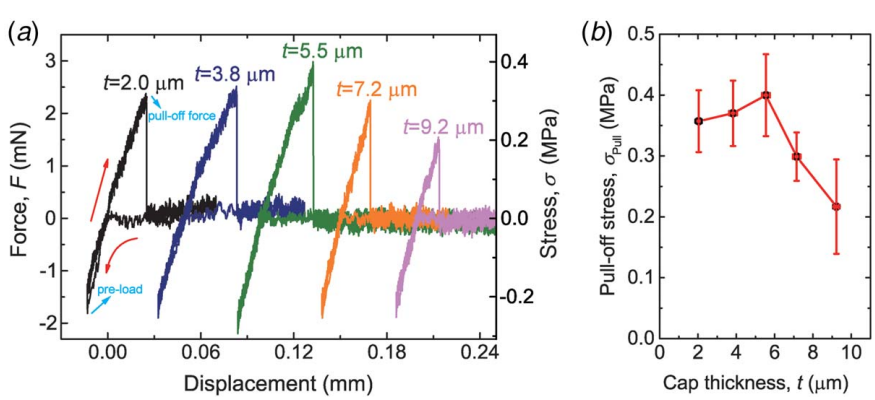

Fig. 3 Adhesion tests. (*a*) The force–displacement curves of all fibrils with varying cap thicknesses from 2.0 μm (left most) to 9.2 μm (right most). The compressive preload was about −2 mN. (*b*) Pull-off stresses σ_{Pull} obtained from the experiments as a function of the cap thickness. Error bars represent the standard deviation.

Downloaded from http://asmedigitalcollection.asme.org/appliedmechanics/article-pdf/88/3/031015/6624836/jam_88_3_031015.pdf by guest on 20 August 2022

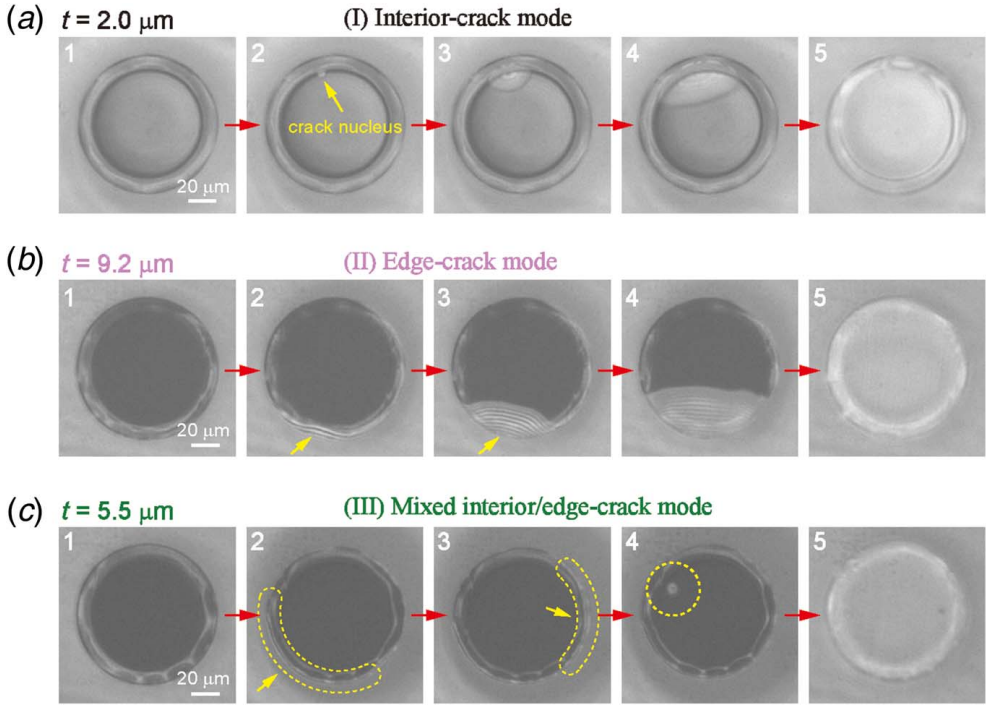

Fig. 4 Snapshots taken during the retraction of fibrils with various cap thicknesses: (1) adhesive contact at preload, (2) first crack nucleus, (3 and 4) propagation of the crack, and (5) detached. Cracks and detachment varied depending on the cap thickness: (*a*) $t = 2.0$ μm: the interior-crack mode, (*b*) $t = 9.2$ μm: edge-crack mode, and (c) $t = 5.5$ μm: mixed interior/edge-crack mode.

in the adhesion experiments, the variation of adhesion is related to that structural modification.

By observing the adhesive contact during retraction of the fibrils, we found three characteristic modes of detachment, as displayed in Fig. 4:

- *Mode I—Interior-Crack Mode*: This mode was found for thin mushroom caps of thickness 2.0 and 3.8 μm. For $t = 2.0$ μm, snapshots captured during detachment exhibited an interfacial crack nucleus (bright spot) below the transition from the stalk to the cap (pointed by arrow in Fig. 4(*a*-2)). The crack propagated both inward and outward until the microfibril separated from the glass probe. Such a characteristic detachment is referred to as interior-crack mode because the crack was initiated within the contact area.
- *Mode II—Edge-Crack Mode*: Mode II was found for thick caps of thickness 7.2 and 9.2 μm. Here, the fibrils detached from the outer edge of the contact with a crack propagating inward, as shown in Fig. 4(*b*). The crack propagation appeared as growing diffraction fringes due to the monochromatic light source.
- *Mode III—Mixed Interior/Edge-Crack Mode*: This mode was found only for the intermediate cap thickness of $t = 5.5$ μm. Interfacial crack propagation was by a mixed mode of interior and edge cracks, as shown in Fig. 4(*c*). First, edge cracks formed at two opposite positions as highlighted by the areas enclosed by dashed curves in Fig. 4(*c*-2 and *c*-3). However, these cracks stopped to propagate while another crack nucleated below the stalk that promptly caused detachment.

5 Simulation Results

5.1 Pull-Off Forces and Interfacial Stress Distributions. For the finite element analysis, normalized values were introduced as follows:

$$\bar{f} = \frac{4f}{\pi D_L^2 \sigma_0},\ \bar{d} = \frac{d}{H},\ \bar{t} = \frac{t}{D_L},\ \bar{r} = \frac{2r}{D_L},\ \text{and}\ \bar{\sigma} = \frac{\sigma_{yy}}{\sigma_0} \tag{3}$$

where f and d are the actual force and displacement exerted from the simulations at the top surface of the fibril, r is the distance along the interface from the edge toward the center of the fibril (Fig. 2(*a*)), and σ_{yy} is the tensile stress distributed across the interface between the cap and the substrate.

Figure 5(*a*) depicts the normalized force–displacement curves for $D_S/D_L = 0.8$ and the cap thickness t/D_L ranging from 0.008 to 0.10, which was chosen in accordance with the dimensions in the experiments. In all the curves, $\bar{f}$ increased linearly until the maximum force, $\bar{f}_{\text{pull}}$ was reached. Upon exceeding $\bar{f}_{\text{pull}}$, the force dropped drastically to zero related to the detachment of the fibril from the substrate accompanied with the deletion of all cohesive zone elements. The slope of the force–displacement curve in the linear regime was similar for all designs, as variations of the cap design do not significantly alter the stiffness of the fibril. Figure 5(*b*) depicts the normalized pull-off force $\bar{f}_{\text{pull}}$ as a function of the normalized cap thickness $\bar{t}$ (dots linked to the left y-axis). The force increased with the increasing cap thicknesses up to a maximum of 0.68 for $\bar{t} = 0.07$, and then, $\bar{f}_{\text{pull}}$ decreased again. The trend was similar to that observed in the experiments, where we found a maximum for $t = 5.5$ μm, i.e., $\bar{t} = 0.055$ (dots linked to the right y-axis in Fig. 5(*b*)). The good agreement between FEA and experimental results depends on the choice of σ_0 in the cohesive zone model (see Appendix A).

For the different cap thicknesses $\bar{t} = 0.008$, 0.07, and 0.1, the evolution of the interfacial stress distribution during the detachment is displayed in log-log plots in Fig. 6. The five interfacial stress curves displayed in the right column correspond to five moments in the force–displacement curves marked by circle dots (A–E) in Figs. 6(*a*), 6(*c*), and 6(*e*). For the thin cap with $\bar{t} = 0.008$, the interfacial tensile stresses at the edge ($\bar{r} \approx 10^{-5}$) were 2 orders of magnitude smaller than the stresses below the stalk ($\bar{r} \approx 1$) (Fig. 6(*b*)). In addition, a stress concentration and therefore the maximum interfacial stress was located below the transition from the stalk to the cap. This result is in accordance with the previous studies [23,25] and confirms that thin caps effectively decrease the magnitude of the stress singularity at the corner. Thus, detachment from the

Downloaded from http://asmedigitalcollection.asme.org/appliedmechanics/article-pdf/88/3/031015/6624836/jam_88_3_031015.pdf by guest on 20 August 2022

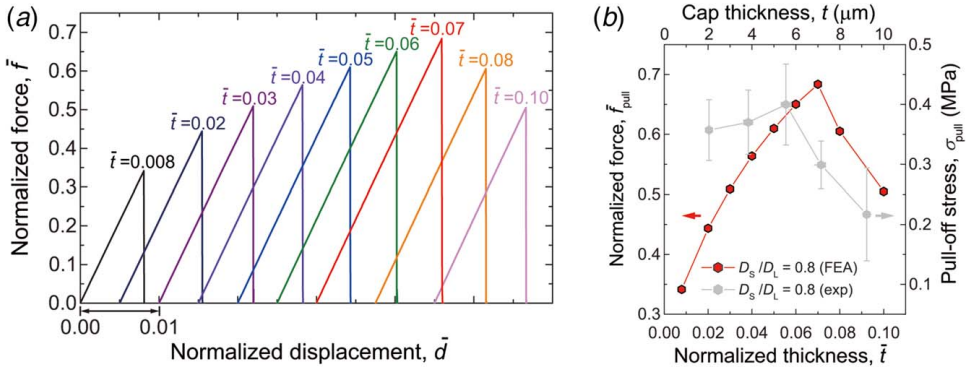

Fig. 5 FEA results: (*a*) normalized force–displacement curves of the mushroom cap fibrils with normalized cap thickness $0.008 \le \bar{t} \le 0.10$ and (*b*) normalized $\bar{f}_{pull}$ (obtained from FEA) in terms of $\bar{t}$ for the diameter ratio of the stalk to the cap $D_S/D_L = 0.8$ (dots linked to the left *y*-axis) in comparison to the experimentally obtained pull-off stresses (dots linked to the right *y*-axis).

edge of the cap is suppressed until the pull-off force $\bar{f}_{Pull}$ is reached (point E).

With the increasing cap thickness, the magnitude of the edge stress singularity increased, whereas the stresses below the stalk slightly decreased. For the very thick cap with $\bar{t} = 0.1$, the edge stress dominated (Fig. 6(*d*)). As $\bar{f}$ increased during pulling of the fibril, the stress at the edge decreased, as the damage parameter D of the relevant cohesive elements increased. As a consequence, the stress peak moved slightly inward into the contact. Similarly, the interfacial stress below the stalk increased with the increasing loading $\bar{f}$. However, at pull-off (point E), the maximum tensile stress was located at $\bar{r} = 0.02$, i.e., near the edge, leading to edge-crack detachment in accordance with the experiment (see Fig. 4(*b*)).

The evolution of the interfacial stress distributions for $\bar{t} = 0.07$ led to the highest pull-off force of 0.68 as shown in Fig. 6(*e*). At point A, the stress gradient was initially present at the edge of the cap and the tensile stresses below the stalk were about half of the stress at the edge. During further loading of the fibril, the peak stress moved from the edge into the contact, whereas the stress at the edge dropped due to an increase in the damage parameter D. This is in accordance to the observations in the experiments, where the fibril detached locally from the edge of the cap (compare moments 2 and 3 captured in Fig. 4(*c*)). With the ongoing loading of the fibril, the stresses below the stalk finally exceeded the peak stress close to the edge (see point E in Fig. 6(*f*)). Thus, the crack propagated less from the edge, but a new crack was formed below the fibril stalk in line with the experiments (see moment 4 in Fig. 4(*c*)).

5.2 Influence of the Stalk Diameter and Young's Modulus.

To further investigate possible designs, simulations with different stalk diameters and cap thickness were conducted. This study included D_S/D_L ranging from 0.6 to 0.9 and $\bar{t}$ ranging from 0.1 to 1.5. Figure 7(*a*) displays $\bar{f}_{pull}$ in terms of $\bar{t}$. Each curve for a constant D_S/D_L shows a similar trend with a maximum pull-off force, as described earlier. For thicker stalks, i.e., for larger ratio D_S/D_L, the optimal $\bar{t}$ becomes smaller (Fig. 7(*b*)). Conversely, this means that a mushroom fibril with a fixed cap diameter, but a thinner stalk would need a thicker cap to achieve optimal adhesion. As a result, when the optimal pull-off force appears with a fixed D_S/D_L, the length of cap u, and cap thickness t are comparable to some extent. For a given Young's modulus, the ratio of the optimal t to the cap length u for different D_S/D_L always fluctuated around a constant, which is relevant to Young's modulus (Fig. 7(*c*)). Interestingly, the maximum $\bar{f}_{pull}$ for different D_S/D_L did not change monotonically with the increasing D_S/D_L (Fig. 7(*d*)). In our simulations, the largest adhesion force was found for $D_S/D_L = 0.8$, which gives the optimal ratio of the stalk to cap diameter (Fig. 7(*d*)).

The elastic modulus of the fibril is another important parameter to be considered. On the basis of FEA, we found two opposite trends. For caps thinner than the optimal thickness, pull-off forces were insensitive to two different Young's moduli used in the simulations. For thicker caps, pull-off forces dropped by 10% when the modulus decreased from 2.52 to 2 MPa. In addition, the optimal thickness slightly shifted to thinner caps when the material was softer.

6 Discussion

Since the early work by Del Campo et al. [7] and Gorb et al. [10], it is well known that mushroom-shaped microfibrils exhibit better and more robust adhesion than flat punches. Intuitively, the addition of thin material flaps as part of a terminal cap is beneficial because the axial tensile stresses along the stalk will translate into more "diffuse" stresses, directed away from the interface, at the cap edge; this "protects" the edge of the cap from the otherwise inevitable singularities. To estimate the extent of this effect, quantitative calculations are necessary. Previous modeling and simulation by Spuskanyuk et al. [23] and Carbone et al. [24] were first attempts to quantify this effect. The interfacial fracture mechanics treatment by Balijepalli et al. [25] was the first to associate a decreasing cap thickness with a decreased magnitude of the stress singularity; consequently, an increased adhesion stress was anticipated for thinner caps.

In this study, an experimental measurement with in situ observation and a numerical study of this effect have been combined for the first time. As a result, an optimum cap thickness exists for a given ratio of the stalk diameter to the cap diameter and for a given Young's modulus; below this optimum value, the adhesion progressively decreases again. Intuitively, an optimum thickness can be understood as follows: too thick caps will approach the inferior behavior of flat punches, while too thin caps cannot fully smoothen the interfacial stress concentration due to the sharp transition from the stalk to the cap, even a fillet is added to the transitional region (Fig. 8 in Appendix B).

The present analysis of the interfacial stress distributions is consistent with earlier calculations. Previous theoretical analyses have demonstrated that when detaching a compliant flat punch from a rigid substrate, the singular stress field at the edge of the punch plays an important role. If the edge stress exceeds all other interfacial stress values, an edge crack will nucleate and propagate along the interface to separate the contact [21,29]. Similarly, we observed detachment of mushroom fibrils with thick caps from the edge. The interfacial stress distributions obtained from FEA exhibited peak stresses close to the edge of the mushroom cap, which dominated the detachment at low pull-off forces compared to other designs addressed in our study. Therefore, thick caps, i.e., larger than the optimal cap thickness, lead to mushroom fibrils performing similar to flat punches without a cap [25]. This is in good

Downloaded from http://asmedigitalcollection.asme.org/appliedmechanics/article-pdf/88/3/031015/6624836/jam_88_3_031015.pdf by guest on 20 August 2022

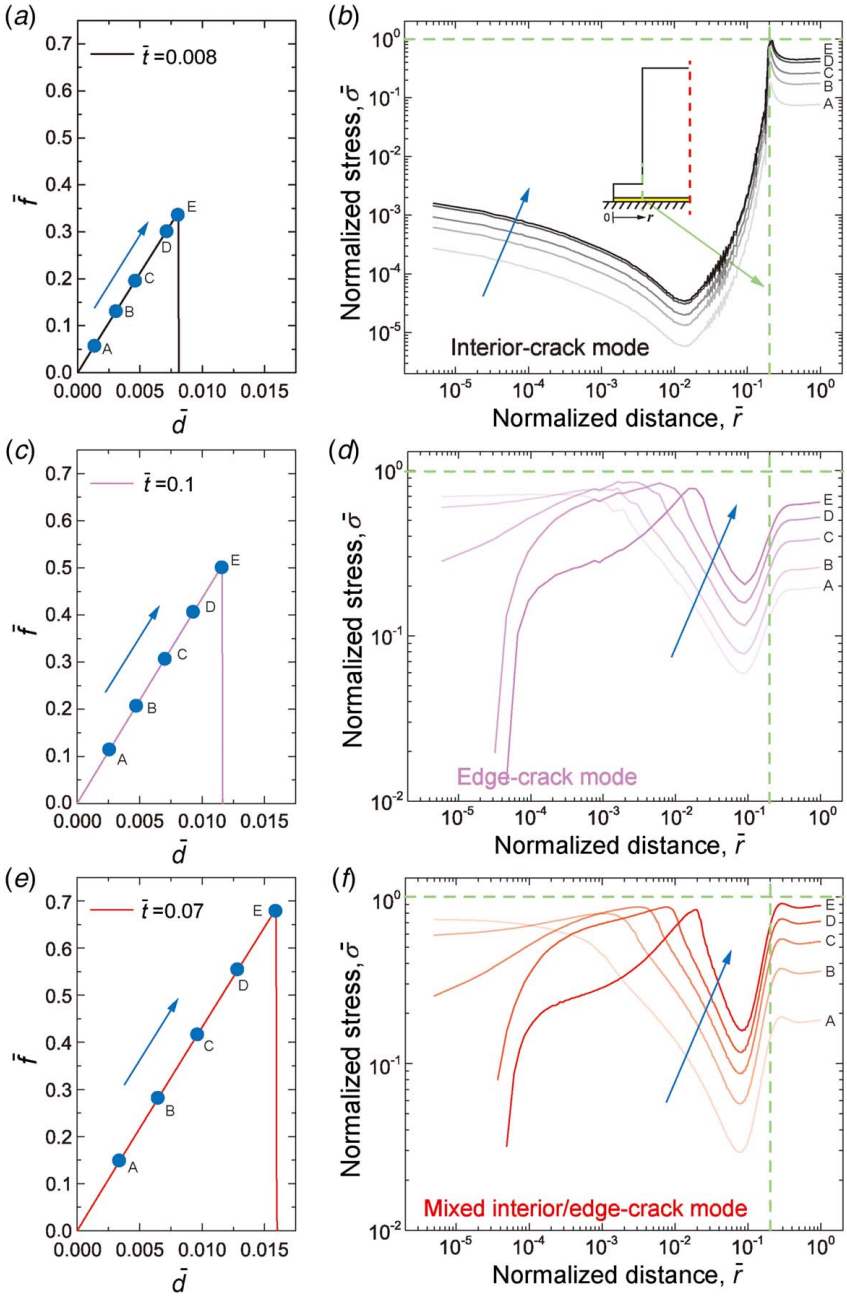

Fig. 6 FEA results of the normalized force–displacement curves (left) and the evolution of the stress distributions along the interface (right) for (*a*) and (*b*) $\bar{t} = 0.008$ with an interior-crack mode, (c) and (*d*) $\bar{t} = 0.1$ with an edge-crack mode, and (e) and (*f*) $\bar{t} = 0.07$ with a mixed interior/edge-crack mode. Blue arrows indicate the evolution of the interfacial stresses with increasing tensile forces from A to E, at which E relates to the pull-off force $\bar{f}_{pull}$. In the stress distribution plots, two dashed guidelines are inserted to highlight the position of the transition from the stalk to the cap (vertical dashed line) and the stress equal to σ_0 defined in the cohesive zone model (horizontal dashed line). (Color version online.)

agreement with our findings, as the detachment from the edge was suppressed for very thin caps, but occurred at the transition from the stalk to the cap (Figs. 4(*a*) and 6(*b*)), at which a stress concentration appeared [23].

On the basis of the aforementioned discussion, there exist two limiting cases where the thickness of the cap is zero or infinite. Therefore, adhesion force saturates with the pull-off force of a flat punch with the diameter D_S or D_L, which in both cases is dominated by the edge stress singularity. However, the implementation of a finite thick mushroom cap requires an optimal thickness to maximize adhesion. On the basis of our cohesive zone model, we found optimal normalized thickness $\bar{t}$ of 0.07 for the ratio D_S/D_L of 0.8, which leads to a mixed interior/edge mode detachment, which was ignored by most of the previous studies. It should be noted that variations of D_S/D_L lead to changes of the optimal cap thickness and that the optimal thickness is sensitive to the elastic modulus. However, the optimal ratio D_S/D_L is always about 0.8. Interestingly, this result agrees with similar studies on conical-shaped mushroom caps conducted by Aksak et al. [26] (see Appendix C). The authors found an optimal ratio $0.8 \leq D_S/D_L \leq 0.9$ for a conical angle of 45 deg in the simulations [26] and D_S/D_L ranging between 0.71 and 0.83 in the experiments [16],

Downloaded from http://asmedigitalcollection.asme.org/appliedmechanics/article-pdf/88/3/031015/6624836/jam_88_3_031015.pdf by guest on 20 August 2022

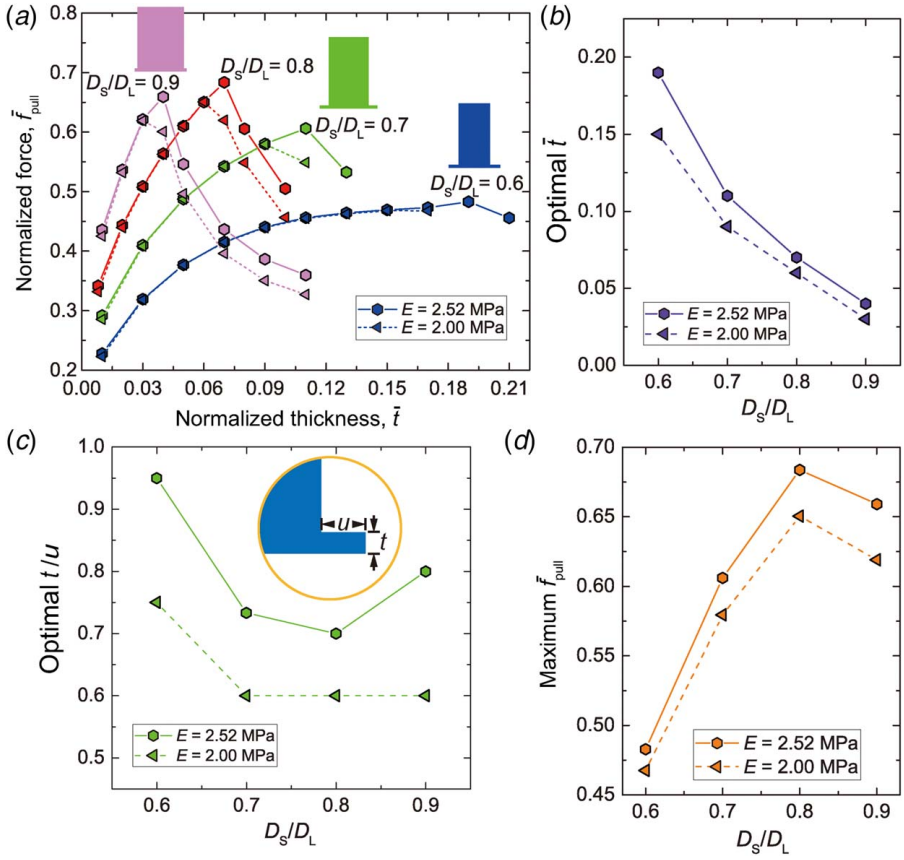

Fig. 7 Variation of the stalk diameter/cap diameter ratio, D_S/D_L, and of Young's modulus. (*a*) Normalized pull-off forces $\bar{f}_{Pull}$ versus normalized cap thickness $\bar{t}$ for mushroom-shaped fibrils with D_S/D_L ranging from 0.6 (right most) to 0.9 (left most). The results are shown for a Young's modulus E of 2.52 MPa (hexagons) and 2 MPa (triangles). (*b*) Optimal $\bar{t}$ obtained from (*a*) as a function of D_S/D_L for $E = 2$ and 2.52 MPa. (*c*) The ratio of optimal t to cap length u (shown in inset) changing with D_S/D_L for $E = 2$ and 2.52 MPa. (*d*) Maximum $\bar{f}_{Pull}$ as a function of D_S/D_L for $E = 2$ and 2.52 MPa, demonstrating the optimal design for $D_S/D_L = 0.8$.

which confirms rather short mushroom flaps. For comparison of the adhesion performance between conical shape cap and flat shape cap, we simulated their optimal design by using our material parameters and cohesive zone model (Fig. 9). The results gave a normalized pull-off force of 0.63 and 0.78 (Table 1) depending on the presence of a thin disc to capture fabrication inaccuracies, which is in good agreement with our maximum $\bar{f}_{pull}$ of 0.68. In an earlier work, Carbone and Pierro [30] obtained the best performance of a mushroom fibril for $D_S/D_L = 0.33 \sim 0.5$ and $\bar{t} \approx 0.1$. This finding of optimal $\bar{t}$ is consistent with our results when D_S/D_L is chosen between 0.3 and 0.5. However, they ignored cases of $D_S/D_L > 0.5$; thus, our research extended the previous work, leading to an optimal choice for D_S/D_L of 0.8.

In the current work, we should notice that all fibrils in the experiments and simulations were large enough to be sensitive to

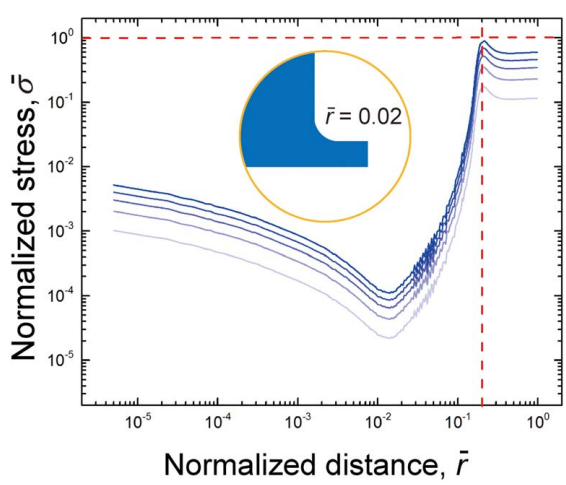

Fig. 8 The evolution of the stress distributions along the interface for mushroom cap fibril with $\bar{t} = 0.008$ and a fillet of normalized radius (fillet radius to cap diameter) of 0.02. The different transparencies of the curves correspond to different instances during detachment.

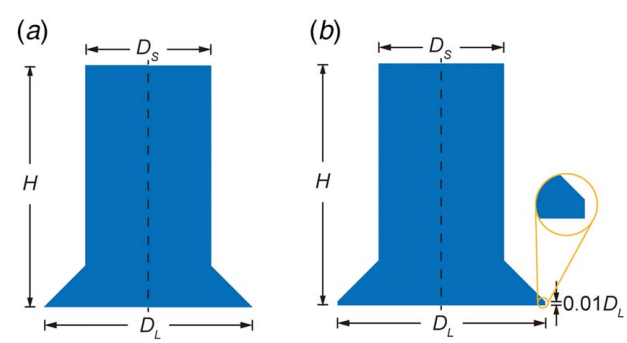

Fig. 9 Schematics of the conical-shaped mushroom fibril. The fibril height is H, the stalk diameter D_S, the tip diameter D_L. Two modifications of the tip were studied: (*a*) without a thin disc and (*b*) with a thin disc at the thickness of $0.01D_L$.

Downloaded from http://asmedigitalcollection.asme.org/appliedmechanics/article-pdf/88/3/031015/6624836/jam_88_3_031015.pdf by guest on 20 August 2022

Table 1 Summary of the normalized pull-off force $\bar{f}_{\text{Pull}}$ of conical-shaped mushroom fibrils without (Fig. 9(*a*)) and with thin disc (Fig. 9(*b*)) for ratios D_S/D_L of 0.83 and 0.91

D_S/D_L	0.83	0.91
Without thin disc	0.78	0.73
With a thin disc	0.63	0.54

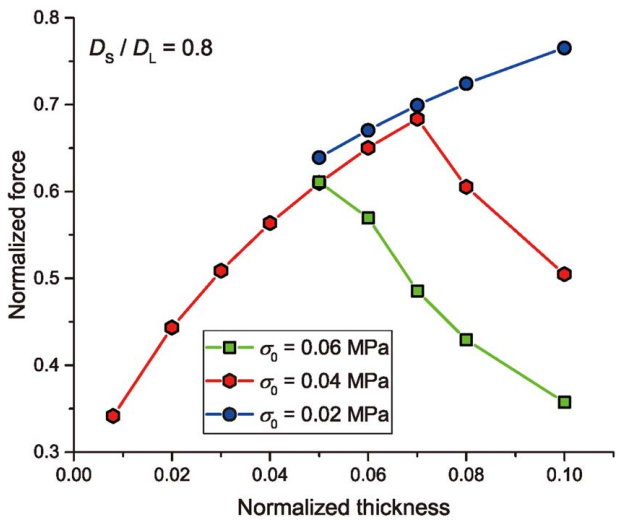

Fig. 10 Normalized force $\bar{f}_{\text{pull}}$ varies with normalized thickness $\bar{t}$ for D_S/D_L = 0.8. Circle, hexagon, and square dots are related to variations of the maximum traction σ_0 = 0.02, 0.04, 0.06 MPa in the cohesive zone model. (Color version online.)

interfacial defects. It has been demonstrated by previous reports that a continuous decreasing of the diameter of the fibril will lead to a transition from a defect-sensitive regime to a defect-insensitive regime [22,31], where the inherent adhesion strength is exactly σ_0 defined in the cohesive zone model and the normalized pull-off force $\bar{f}_{\text{pull}} = 1$. A dimensionless parameter to estimate the transition between the two regimes is expressed as follows [31]:

$$\chi \equiv \frac{\sigma_0^2 D_L}{4\pi E^* W_{\text{ad}}} \approx 0.7 \tag{4}$$

where $E^* \equiv E/(1-\nu^2)$, below which the behavior of the fibril is located in the defect-insensitive regime. By inserting the parameters used in our FEA, $\chi = 10.1$, which is much larger than 0.7 that implies the defect-sensitive regime in our simulations.

7 Conclusion

The combination of numerical analysis, adhesion experiments, and in situ observation revealed the optimal dimensions of the mushroom-shaped fibril for maximal adhesion. The following conclusions can be drawn:

- Cap thickness affects the interfacial stress distribution and the crack mode. Variations of the cap thickness leads to variations of the interfacial stress distribution, leading to different crack modes: thin caps lead to an interior crack that nucleates prematurely at the transition from the stalk to the cap. In contrast, thick caps result in a rapidly propagating edge crack. At the optimal cap thickness, a mixed mode with detachments from the edge and the inner contact were observed, which indicates best load sharing along the interface just before pull-off.
- A new optimum design has been identified: Numerical simulations revealed that the optimal cap thickness varies with the ratio of the stalk diameter to cap diameter D_S/D_L. The maximum pull-off force was obtained for $D_S/D_L = 0.8$ and a cap thickness of $t/D_L = 0.07$. This means that a fibril with a diameter $D_S = 80$ μm requires a cap diameter $D_L = 100$ μm and a cap thickness of 7 μm, which is in accordance with our experiments where the optimal thickness was slightly smaller with 5.5 μm.
- Besides the cap dimensions, the elastic modulus of the material affected adhesion, where a stiffer material led to improved adhesion, but requires a thicker cap. However, the optimal ratio D_S/D_L was still 0.8.

This study also shows that a targeted design of the cap can induce a homogeneous load distribution along the entire interface, resulting in an adhesion strength equivalent to the cohesive strength at the interface.

Acknowledgment

The study leading to these results was funded by the Leibniz Competition Grant MUSIGAND (Grant No. K279/2019).

Conflict of Interest

There are no conflicts of interest.

Data Availability Statement

The datasets generated and supporting the findings of this article are obtainable from the corresponding author upon reasonable request. The data and information that support the findings of this article are freely available online, as are Supplementary Videos 1–3.[2] The authors attest that all data for this study are included in the paper.

Appendix A: The Choice of Parameters in Cohesive Zone Model

We conducted additional simulations on the mushroom cap fibril with $D_S/D_L = 0.8$ to obtain the optimal thickness of the cap by varying the maximum adhesion strength in the cohesive zone model σ_0 from 0.02 to 0.06 MPa. Figure 10 shows that σ_0 affects the value of optimal $\bar{t}$. For larger σ_0, the optimal thickness $\bar{t}$ decreases. Therefore, σ_0 has to be chosen carefully. Furthermore, variations of the contact stiffness K in the cohesive zone model had no influence on the detachment force, as summarized in Table 2.

Appendix B: The Influence of the Additional Fillet to the Stress Distribution

Additional simulations were conducted on mushroom-shaped fibrils with a fillet of radius $\bar{r} = 0.02$ at the transition between the stalk and the cap. Figure 8 shows the evolution of the stress distribution during the detachment. Although the fillet reduces the peak stress in comparison to the results shown in Fig. 6(*a*), the highest stress values still appear below the transition from the stalk to the cap.

Appendix C: The Detachment Behavior of the Conical-Shaped Mushroom Fibril

Conical-shaped mushroom fibrils were studied to compare our optimized design with the optimized design reported in Ref. [26] by means of an identical cohesive zone model.

[2]https://github.com/mollyxiaoxuan/A-Design-Strategy-for-Mushroom-Shaped-Microfibrils- with-Optimized-Dry-Adhesion-Experiments-and-Fini

Downloaded from http://asmedigitalcollection.asme.org/appliedmechanics/article-pdf/88/3/031015/6624836/jam_88_3_031015.pdf by guest on 20 August 2022

Table 2 The influence of contact stiffness K on the normalized pull-off force $\bar{f}_{\mathrm{Pull}}$

	Normalized force $\bar{f}_{\mathrm{Pull}}$		
K (N/mm)	$\bar{t} = 0.02$	$\bar{t} = 0.07$	$\bar{t} = 0.1$
1×10^5	0.44	0.68	0.51
4×10^5	0.44	0.68	0.50
1×10^6	0.44	0.68	0.51

References

[1] Hensel, R., Moh, K., and Arzt, E., 2018, "Engineering Micropatterned Dry Adhesives: From Contact Theory to Handling Applications," Adv. Funct. Mater., **28**(28), p. 1800865.

[2] Li, Y., Ahmed, A., Sameoto, D., and Menon, C., 2012, "Abigaille II: Toward the Development of a Spider-Inspired Climbing Robot," Robotica, **30**(1), pp. 79–89.

[3] Kim, S., Spenko, M., Trujillo, S., Heyneman, B., Santos, D., and Cutkosky, M. R., 2008, "Smooth Vertical Surface Climbing With Directional Adhesion," IEEE Trans. Robot., **24**(1), pp. 65–74.

[4] Autumn, K., Liang, Y. A., Hsieh, S. T., Zesch, W., Chan, W. P., Kenny, T. W., Fearing, R., and Full, R. J., 2000, "Adhesive Force of a Single Gecko Foot-Hair," Nature, **405**(6787), pp. 681–685.

[5] Arzt, E., Gorb, S., and Spolenak, R., 2003, "From Micro to Nano Contacts in Biological Attachment Devices," Proc. Natl. Acad. Sci. USA, **100**(19), pp. 10603–10606.

[6] Federle, W., 2006, "Why Are so Many Adhesive Pads Hairy?," J. Exp. Biol., **209**(14), pp. 2611–2621.

[7] Del Campo, A., Greiner, C., and Arzt, E., 2007, "Contact Shape Controls Adhesion of Bioinspired Fibrillar Surfaces," Langmuir, **23**(20), pp. 10235–10243.

[8] Heepe, L., and Gorb, S. N., 2014, "Biologically Inspired Mushroom-Shaped Adhesive Microstructures," Annu. Rev. Mater. Res., **44**(1), pp. 173–203.

[9] Bullock, J. M. R., and Federle, W., 2011, "Beetle Adhesive Hairs Differ in Stiffness and Stickiness: In Vivo Adhesion Measurements on Individual Setae," Naturwissenschaften, **98**(5), pp. 381–387.

[10] Gorb, S., Varenberg, M., Peressadko, A., and Tuma, J., 2007, "Biomimetic Mushroom-Shaped Fibrillar Adhesive Microstructure," J. R. Soc. Interface, **4**(13), pp. 271–275.

[11] Fischer, S. C. L., Groß, K., Torrents Abad, O., Becker, M. M., Park, E., Hensel, R., and Arzt, E., 2017, "Funnel-Shaped Microstructures for Strong Reversible Adhesion," Adv. Mater. Interfaces, **4**(20), p. 1700292.

[12] Fischer, S. C. L., Arzt, E., and Hensel, R., 2017, "Composite Pillars With a Tunable Interface for Adhesion to Rough Substrates," ACS Appl. Mater. Interfaces, **9**(1), pp. 1036–1044.

[13] Murphy, M. P., Aksak, B., and Sitti, M., 2007, "Adhesion and Anisotropic Friction Enhancements of Angled Heterogeneous Micro-Fiber Arrays With Spherical and Spatula Tips," J. Adhes. Sci. Technol., **21**(12), pp. 1281–1296.

[14] Wang, Y., Kang, V., Arzt, E., Federle, W., and Hensel, R., 2019, "Strong Wet and Dry Adhesion by Cupped Microstructures," ACS Appl. Mater. Interfaces, **11**(29), pp. 26483–26490.

[15] Tinnemann, V., Hernández, L., Fischer, S. C. L., Arzt, E., Bennewitz, R., and Hensel, R., 2019, "In Situ Observation Reveals Local Detachment Mechanisms and Suction Effects in Micropatterned Adhesives," Adv. Funct. Mater., **29**(14), p. 1807713.

[16] Marvi, H., Song, S., and Sitti, M., 2015, "Experimental Investigation of Optimal Adhesion of Mushroomlike Elastomer Microfibrillar Adhesives," Langmuir, **31**(37), pp. 10119–10124.

[17] Tinnemann, V., Arzt, E., and Hensel, R., 2019, "Switchable Double-Sided Micropatterned Adhesives for Selective Fixation and Detachment," J. Mech. Phys. Solids, **123**, pp. 20–27.

[18] Heepe, L., Kovalev, A. E., Filippov, A. E., and Gorb, S. N., 2013, "Adhesion Failure at 180 000 Frames Per Second: Direct Observation of the Detachment Process of a Mushroom-Shaped Adhesive," Phys. Rev. Lett., **111**(10), p. 104301.

[19] Kroner, E., and Arzt, E., 2013, "Mechanistic Analysis of Force-Displacement Measurements on Macroscopic Single Adhesive Pillars," J. Mech. Phys. Solids, **61**(6), pp. 1295–1304.

[20] Khaderi, S. N., Fleck, N. A., Arzt, E., and McMeeking, R. M., 2015, "Detachment of an Adhered Micropillar From a Dissimilar Substrate," J. Mech. Phys. Solids, **75**, pp. 159–183.

[21] Gao, H., Wang, X., Yao, H., Gorb, S., and Arzt, E., 2005, "Mechanics of Hierarchical Adhesion Structures of Geckos," Mech. Mater., **37**(2), pp. 275–285.

[22] Gao, H., and Yao, H., 2004, "Shape Insensitive Optimal Adhesion of Nanoscale Fibrillar Structures," Proc. Natl. Acad. Sci. USA, **101**(21), pp. 7851–7856.

[23] Spuskanyuk, A. V., McMeeking, R. M., Deshpande, V. S., and Arzt, E., 2008, "The Effect of Shape on the Adhesion of Fibrillar Surfaces," Acta Biomater., **4**(6), pp. 1669–1676.

[24] Carbone, G., Pierro, E., and Gorb, S. N., 2011, "Origin of the Superior Adhesive Performance of Mushroom-Shaped Microstructured Surfaces," Soft Matter, **7**(12), pp. 5545–5552.

[25] Balijepalli, R. G., Begley, M. R., Fleck, N. A., McMeeking, R. M., and Arzt, E., 2016, "Numerical Simulation of the Edge Stress Singularity and the Adhesion Strength for Compliant Mushroom Fibrils Adhered to Rigid Substrates," Int. J. Solids Struct., **85**, pp. 160–171.

[26] Aksak, B., Sahin, K., and Sitti, M., 2014, "The Optimal Shape of Elastomer Mushroom-Like Fibers for High and Robust Adhesion," Beilstein J. Nanotechnol., **5**(1), pp. 630–638.

[27] Purtov, J., Verch, A., Rogin, P., and Hensel, R., 2018, "Improved Development Procedure to Enhance the Stability of Microstructures Created by Two-Photon Polymerization," Microelectron. Eng., **194**, pp. 45–50.

[28] ABAQUS 6.14 Documentation, 2014, *Dassault Systems*, Simulia Corporation, Providence, RI.

[29] Fleck, N. A., Khaderi, S. N., McMeeking, R. M., and Arzt, E., 2017, "Cohesive Detachment of an Elastic Pillar From a Dissimilar Substrate," J. Mech. Phys. Solids, **101**, pp. 30–43.

[30] Carbone, G., and Pierro, E., 2012, "Sticky Bio-Inspired Micropillars: Finding the Best Shape," Small, **8**(9), pp. 1449–1454.

[31] Tang, T., Hui, C. Y., and Glassmaker, N. J., 2005, "Can a Fibrillar Interface Be Stronger and Tougher Than a Non-Fibrillar One," J. R. Soc. Interface, **2**(5), pp. 505–516.

Downloaded from http://asmedigitalcollection.asme.org/appliedmechanics/article-pdf/88/3/031015/6624836/jam_88_3_031015.pdf by guest on 20 August 2022